

## Observed 10–20-Day Deep-Current Variability at 5°N, 90.5°E in the Eastern Indian Ocean

JINGHONG WANG,<sup>a,b</sup> YEQIANG SHU<sup>a</sup>,<sup>b</sup> DONGXIAO WANG,<sup>c</sup> JU CHEN,<sup>a</sup> YANG YANG,<sup>d</sup> WEIQIANG WANG,<sup>a</sup> BINBIN GUO,<sup>e</sup> KE HUANG,<sup>a</sup> AND YUNKAI HE<sup>a,b</sup>

<sup>a</sup> State Key Laboratory of Tropical Oceanography, South China Sea Institute of Oceanology, Chinese Academy of Sciences, Guangzhou, China

<sup>b</sup> University of Chinese Academy of Sciences, Beijing, China

<sup>c</sup> School of Marine Sciences, Sun Yat-sen University, Guangzhou, China

<sup>d</sup> School of Marine Sciences, Nanjing University of Information Science and Technology, Nanjing, China

<sup>e</sup> National Engineering Research Center of Gas Hydrate Exploration and Development, Guangzhou Marine Geological Survey, Guangzhou, China

(Manuscript received 11 May 2023, in final form 6 November 2023, accepted 28 November 2023)

**ABSTRACT:** In the eastern off-equatorial Indian Ocean, deep current intraseasonal variability within a typical period of 10–20 days was revealed by a mooring at 5°N, 90.5°E, accounting for over 50% of the total bottom subtidal velocity variability. The 10–20-day oscillations were more energetic in the cross-isobathic direction ( $STD = 3.02 \text{ cm s}^{-1}$ ) than those in the along-isobathic direction ( $STD = 1.50 \text{ cm s}^{-1}$ ). The oscillations were interpreted as topographic Rossby waves (TRWs) because they satisfied the TRWs dispersion relation that considered the smaller Coriolis parameter and stronger  $\beta$  effect at low latitude. Further analysis indicated significant vertical coupling between the deep cross-slope oscillations and cross-isobathic 10–20-day perturbations at the depth of 300–950 m. The 10–20-day TRWs were generated by cross-isobathic motions under the potential vorticity conservation adjustment. The Mercator Ocean output reproduced the generation of kinetic energy (KE) of deep current variability. The associated diagnostic analysis of multiscale energetics showed that the KE of TRWs was mainly supplied by vertical pressure work. In the seamount region (2°–10°N, 89°–92°E), vertical and horizontal pressure works were identified to be the dominant energy source (contributing to 94% of the total KE source) and sink (contributing to 98% of the total KE sink) of the deep current variability, transporting energy downward and redistributing energy horizontally, respectively.


**KEYWORDS:** Indian Ocean; Bottom currents; Energy transport; Ocean dynamics; Topographic effects; Intraseasonal variability

### 1. Introduction

Topographic Rossby waves (TRWs) are subinertial waves characterized by periods that span from several days to several hundreds of days and wavelengths ranging from tens to several hundreds of kilometers (Rhines 1970; Oey and Lee 2002). In recent decades, TRWs have been observed in deep ocean regions worldwide. These regions include the northwest Atlantic (Thompson 1971; Thompson and Luyten 1976), the northwest Pacific (Miyamoto et al. 2020), the Arctic Ocean (Zhao and Timmermans 2018), the Gulf of Mexico (GoM; Hamilton 2007, 2009), South China Sea (SCS; Shu et al. 2016; Q. Wang et al. 2019; Zheng et al. 2021b; Shu et al. 2022), East China Sea (ECS; Chen et al. 2022), Japan Sea (Shin et al. 2020), and Philippine Sea (Ma et al. 2019). TRWs are commonly regarded as the prevailing oscillating pattern of subinertial variability in deep oceans (e.g., Thompson and Luyten 1976; Johns and Watts 1986; Hamilton 1990, 2007, 2009; Oey and Lee 2002; Zheng et al. 2021a). For instance, TRWs could

explain over 40% of the total deep current variance over rough topographic region in the SCS according to mooring observations and numerical studies conducted in that region (Q. Wang et al. 2019; Wang et al. 2021; Quan et al. 2021a) and accounted for more than 80% of the total deep-current variance in the GoM based on observations (Hamilton 2009). The excitation of TRWs occurs due to cross-isobathic motion, where fluid columns are stretched or compressed over sloping topography under the adjustment of potential vorticity (PV) conservation (Rhines 1970; Oey and Lee 2002). Previous studies have elucidated that upper-layer intraseasonal variability can act as the energy reservoir of TRWs, such as the Loop Current (LC) and LC eddies in the GoM (Hamilton 1990, 2007; Zhu and Liang 2020), Kuroshio intrusion (Quan et al. 2021b) and the upper-ocean eddies in the northern SCS (Q. Wang et al. 2019; Zheng et al. 2021a), and the Kuroshio meanders (Chen et al. 2022) in the ECS.

In the Northern Hemisphere tropical Indian Ocean, the upper-ocean circulation exhibits strong intraseasonal variations, which are mainly influenced by atmospheric intraseasonal oscillations (e.g., the Madden–Julian oscillation; Madden and Julian 1971; Hendon and Glick 1997; Webster et al. 2002; Shinoda et al. 2013). Off the equatorial regions, such as the Bay of Bengal, certain intraseasonal signals like variations in thermocline and sea surface height can be attributed to

 Denotes content that is immediately available upon publication as open access.

Corresponding author: Ye qiang Shu, shuyeq@scsio.ac.cn

DOI: 10.1175/JPO-D-23-0082.1

© 2024 American Meteorological Society. This published article is licensed under the terms of the default AMS reuse license. For information regarding reuse of this content and general copyright information, consult the AMS Copyright Policy ([www.ametsoc.org/PUBSReuseLicenses](http://www.ametsoc.org/PUBSReuseLicenses)).

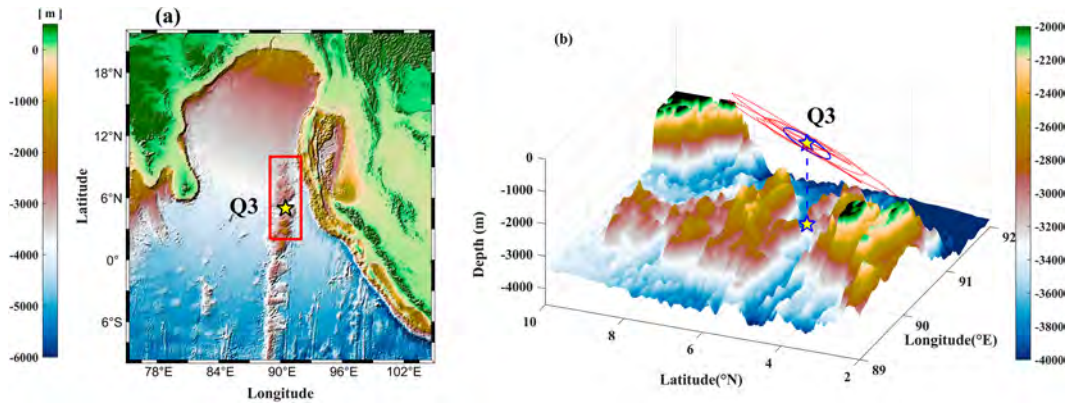


FIG. 1. The study region. (a) Mooring location. (b) Topography of the seamount region. The yellow star represents the location of mooring Q3. The red box indicates the seamount region ( $2^{\circ}$ – $10^{\circ}$ N,  $89^{\circ}$ – $92^{\circ}$ E). The red dotted line in (b) represents the scatterplot of zonal and meridional bottom flows from 28 Aug to 10 Nov 2017. The blue line in (b) depicts the standard deviation ellipse derived from the 10–20-day bandpass-filtered velocities.

remote equatorial intraseasonal winds. This is achieved through the propagation of equatorial Kelvin waves (KWs) and the reflection of coastal KWs, which subsequently transform into westward-propagating Rossby waves (RWs) (Cheng et al. 2013; Girishkumar et al. 2013). Chen et al. (2017) observed strong 30–50-day meridional currents above  $\sim 150$  m at  $5^{\circ}$ N,  $90.5^{\circ}$ E, where the topography is steep; mooring Q3 used in the present study was located in this region (Fig. 1a). The 30–50-day variability of near-surface currents is linked to westward-propagating RWs, which are mainly induced by equatorial wind forcing and equatorial KWs reflection at the eastern boundary. These abundant oceanic wave processes and complex topography of off-equatorial regions (e.g., around mooring Q3) provide conducive conditions to TRW generation in the deep ocean. The response of deep currents to complex topography, and whether TRWs exist in this area is still an unknown scientific question. Owing to the absence of direct observational data, our understanding of the variability of deep currents in this region is currently limited.

Recently, there has been a growing interest in the study of deep-ocean energy pathways and oceanic processes (e.g., D. Wang et al. 2019). As vertical downward energy transport has been frequently reported (Huang et al. 2018, 2020; Chen et al. 2022; Ma et al. 2022), vertical pressure work (PW) is acknowledged as the primary energy source in the deep ocean based on numerical studies (e.g., Maslo et al. 2020; Yang et al. 2021; Quan et al. 2022). TRWs are widely believed to play a pivotal role in the energy transfer pathway from the upper to the deep ocean. For instance, part of the energy originating from upper mesoscale perturbations is transferred to TRWs and redistributed in the deep ocean via TRW propagation (Hamilton 2009; Oey and Lee 2002; Q. Wang et al. 2019; Wang et al. 2021). That is to say, TRWs are the result of the vertical connection of energy between the upper and deep ocean, gain the energy transferred in the vertical direction, and further redistribute the energy horizontally. In some cases, the vertical coupling between the upper and bottom currents can be attributed to the formation of TRWs

(Q. Wang et al. 2019; Zhu and Liang 2020). Therefore, detailed information on dynamics associated with TRWs is essential to understanding deep current variability and energy pathways in this region.

With the feasibility of more extensive measurements in recent years, data on both upper and deep currents are now available from a long-term deep mooring station located at around  $5^{\circ}$ N,  $90.5^{\circ}$ E (yellow star in Fig. 1a). Strong intraseasonal variability of deep currents with a typical period of 10–20 days is observed in both along- and cross-slope directions (Fig. 2). Therefore, the principal aim of this research is to comprehend the 10–20-day deep-current variability and elucidate the underlying dynamics from the perspective of energetics. The remaining sections of the article are structured as follows. Section 2 offers an extensive account of the data and methodologies employed in the study. Subsequently, section 3 presents the results derived from the analysis of data. Section 4 discusses the findings. Finally, section 5 provides a summary.

## 2. Data and methods

### a. Data

A mooring (Q3), referred to as Q3, was installed in the southern Bay of Bengal at around  $5^{\circ}$ N,  $90.5^{\circ}$ E (as shown in Fig. 1a). The deployment site is characterized by numerous seamounts and steep and complex topography (Fig. 1b). The mooring is equipped with two 75-kHz upward-looking acoustic Doppler current profilers (ADCPs) in the upper ocean and a NORTEK Aquadopp current meter at the bottom. The NORTEK Aquadopp current meter recorded the bottom velocity data for over 3 years (from 28 March 2016 to 10 May 2019) at the water depth of  $\sim 3306$  m ( $\sim 30$  m above the seafloor), and the ADCPs measured the velocity profiles for approximately 1 year (from 16 March 2017 to 15 February 2018) over the depth from 39 to 948 m with a vertical interval of 8 m. The velocities from the current meter and ADCPs were sampled at intervals of 600 and 3600 s, respectively. To ensure

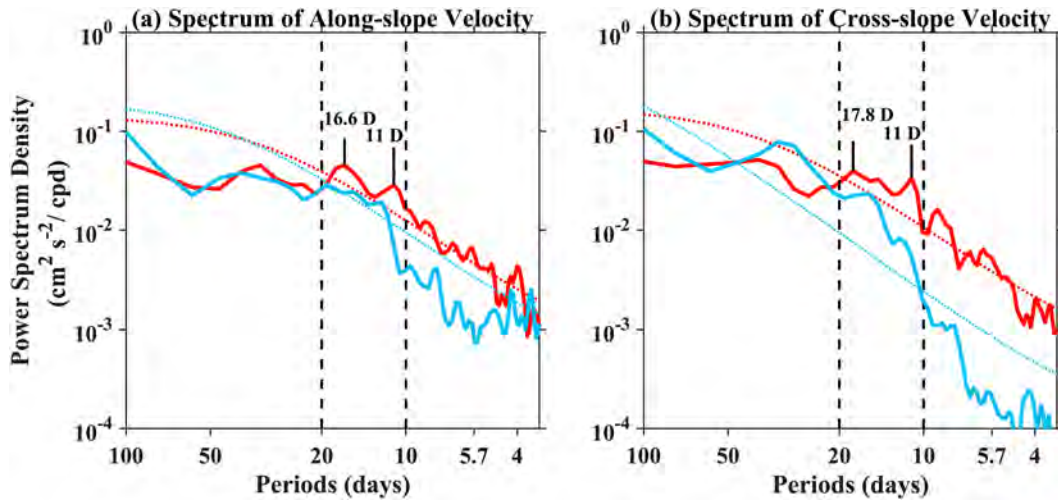


FIG. 2. Power spectrum analysis of the bottom velocities. The results of (a) along-isobathic and (b) cross-isobathic velocities were obtained from observations (red solid line) and Mercator Ocean output (blue solid line) at mooring Q3, respectively. The 95% confidence level based on the red noise test is indicated by the dotted lines.

data quality, the observed velocities underwent essential quality assurance procedures. Any short gaps in the data, typically lasting a few hours and caused by suspect data or mooring redeployment, were filled using linear interpolation. Next, a fourth-order Butterworth bandpass filter with a cutoff frequency of 0.33 cpd (i.e., period of 3 days), was applied to velocities data to eliminate tidal effect. Then, the current data were averaged on a daily basis to obtain the daily zonal ( $U$ ) and meridional ( $V$ ) velocities. Subsequently, the velocity components were rotated for further analysis. The zonal component ( $U$ ) was transformed into the parallel component ( $u$ ) to the isobaths, while the meridional component ( $V$ ) was transformed into the perpendicular component ( $v$ ) to the isobaths. In this context, the raw data were represented by  $u$  and  $v$ , respectively, with a negative  $v$  value implying downslope direction. The downslope direction was determined by the smoothed bathymetry data with a  $50 \times 50 \text{ km}^2$  area average.

To investigate the correlation between upper-ocean meso-scale variability and deep current variability during the observation period, we employed the  $0.25^\circ \times 0.25^\circ$  sea surface geostrophic current anomaly data with a 1-day temporal resolution from the French Archiving, Validation, and Interpretation of Satellite Oceanographic dataset (AVISO; Ducet et al. 2000). The  $1/60^\circ \times 1/60^\circ$  topography data obtained from ETOPO1 (Amante and Eakins 2009) were utilized to calculate the slope and the downslope direction. The  $0.25^\circ \times 0.25^\circ$  climatological hydrographic field from the *World Ocean Atlas 2018* (WOA18) was used to calculate the abyssal Brunt–Väisälä frequency ( $N$ ), which was depth averaged from 3000 to 3300 m in this study.

Because of the limited data of a single mooring, the daily output of velocity during 2014–19 from the Global Mercator Ocean Reanalysis (GLORYS12) product (Lellouche et al. 2018) with  $1/12^\circ$  horizontal resolution and 50 vertical levels, was used to investigate the energy transfer of deep-ocean variability and dynamical processes. The Mercator Ocean (MO)

output has been proven to reproduce the activity of TRWs and utilized to diagnose deep-sea dynamics in the Pacific Ocean (Ma et al. 2019).

### b. Multiscale energetics

To explore the energetics of deep current variability in the seamount region around Q3, we adopted multiscale energy and vorticity analysis (MS-EVA; Liang 2016), which has been widely utilized to assess oceanic and atmospheric processes in previous studies (Liang and Robinson 2009; Ma and Liang 2017; Yang et al. 2021; Yang and Liang 2019; Yang et al. 2020; Quan et al. 2021b). The process of scale separation can be achieved by using multiscale window transform (MWT; Liang and Anderson 2007), a method that orthogonally breaks down the function space into multiple subspaces referred to as scale windows. Using MWT, a given time series  $u(t)$  defined on the interval  $[0, 1]$ , can be reconstructed into three temporal-scale windows, as follows:

$$u(t) = \sum_{\varpi=0}^2 u^{\sim\varpi}(t), \quad (1)$$

where  $\varpi = 0, 1, 2$ , corresponding to the fields filtered through low-pass, bandpass, and high-pass methods, and  $u^{\sim\varpi}(t)$  represents the reconstruction of  $u$  within window  $\varpi$ . The term  $u^{\sim\varpi}(t)$  can be expressed as follows:

$$u^{\sim\varpi}(t) = \sum_{n=0}^{2^2-1} \hat{u}_n^{\sim\varpi} \varphi_n^j(t), \quad (2)$$

$$\hat{u}_n^{\sim\varpi} = \int_0^1 u^{\sim\varpi}(t) \varphi_n^j(t) dt, \quad (3)$$

where  $\hat{u}_n^{\sim\varpi}$  denotes the MWT coefficient,  $\varphi(t)$  represents a localized scaling basis,  $j$  ( $j_0 < j_1 < j_2$ ) stands for the scale level, and  $n$  signifies the discrete time increment within the sampled

domain (Liang and Anderson 2007). Equations (3) and (2) constitute the transformation–reconstruction pair of MWT.

By applying this method to the MO reanalysis data, we separated three temporal-scale windows in the present study, namely, the low-frequency background flow window ( $\varpi = 0$ ), TRW window ( $\varpi = 1$ ; discussed later), and synoptic window ( $\varpi = 2$ ). Details regarding the cutoff period for each window are presented in section 4.

Through the application of MWT to the hydrostatic and Boussinesq fluid flow equations, the tendency equation for multiscale kinetic energy (KE) on window  $\varpi$  [ $K^\varpi = (1/2)\widehat{\mathbf{v}}_h \cdot \widehat{\mathbf{v}}_h$ ] and available potential energy (APE) on window  $\varpi$  [ $\text{APE}^\varpi$ ;  $\text{APE}^\varpi = (1/2)c(\widehat{\rho}^\varpi)^2$ , where  $c = g^2/(\rho_0^2 N^2)$ ] can be obtained as follows (Liang 2016):

$$\begin{aligned} \frac{\partial K^\varpi}{\partial t} = & \frac{1}{2} \underbrace{[(\widehat{\mathbf{v}}_h)^\varpi : \nabla \widehat{\mathbf{v}}_h^\varpi - \nabla \cdot (\widehat{\mathbf{v}}_h)^\varpi \cdot \widehat{\mathbf{v}}_h^\varpi]}_{\Gamma_K^\varpi} \\ & + \underbrace{\left\{ -\nabla \cdot \left[ \frac{1}{2} (\widehat{\mathbf{v}}_h)^\varpi \cdot \widehat{\mathbf{v}}_h^\varpi \right] \right\}}_{-\nabla \cdot Q_K^\varpi} + \underbrace{\left[ -\nabla_h \cdot \left( \frac{1}{\rho_0} \widehat{\mathbf{v}}_h^\varpi \widehat{P}^\varpi \right) \right]}_{-\nabla_h \cdot Q_p^\varpi} \\ & + \underbrace{\left[ -\frac{\partial}{\partial z} \left( \frac{1}{\rho_0} \widehat{w}^\varpi \widehat{P}^\varpi \right) \right]}_{-\nabla_z \cdot Q_p^\varpi} + \underbrace{\left( -\frac{g}{\rho_0} \widehat{\rho}_a^\varpi \widehat{w}^\varpi \right)}_{b^\varpi} + F_K^\varpi, \quad (4) \end{aligned}$$

$$\begin{aligned} \frac{\partial \text{APE}^\varpi}{\partial t} = & \frac{c}{2} \underbrace{[(\widehat{\rho}_a)^\varpi \cdot \nabla \widehat{\rho}_a^\varpi - \widehat{\rho}_a^\varpi \nabla \cdot (\widehat{\rho}_a)^\varpi]}_{\Gamma_A^\varpi} \\ & + \underbrace{\left\{ -\nabla \cdot \left[ \frac{1}{2} (c\widehat{\rho}_a)^\varpi (\widehat{\rho}_a)^\varpi \right] \right\}}_{-\nabla \cdot Q_A^\varpi} + \underbrace{\left( \frac{g}{\rho_0} \widehat{\rho}_a^\varpi \widehat{w}^\varpi \right)}_{-b^\varpi} \\ & + \underbrace{\frac{1}{2} \widehat{\rho}_a^\varpi \widehat{w}^\varpi \frac{\partial c}{\partial z}}_{S_A^\varpi} + F_A^\varpi, \quad (5) \end{aligned}$$

where  $\partial K^\varpi/\partial t$  and  $\partial \text{APE}^\varpi/\partial t$  represent the tendencies of  $K^\varpi$  and  $\text{APE}^\varpi$ , the right-hand-side term  $\Gamma_K^\varpi$  ( $\Gamma_A^\varpi$ ) is the cross-scale KE (APE) transfer,  $-\nabla \cdot Q_K^\varpi$  ( $-\nabla \cdot Q_A^\varpi$ ) is the convergence of KE (APE) flux,  $-\nabla_h \cdot Q_p^\varpi$  ( $-\nabla_z \cdot Q_p^\varpi$ ) is horizontal (vertical) pressure flux convergence,  $b^\varpi$  represents buoyancy conversion,  $S_A^\varpi$  denotes the apparent source/sink arising from the nonlinearity of reference stratification, and  $F_K^\varpi$  ( $F_A^\varpi$ ) is a residual term that includes all the effects of external forcing and unresolved subgrid processes. The colon operator ( $:$ ) is defined as follows, for a pair of dyads (e.g.,  $\mathbf{AB}$  and  $\mathbf{CD}$ ),  $(\mathbf{AB}) : (\mathbf{CD}) = (\mathbf{A} \cdot \mathbf{C})(\mathbf{B} \cdot \mathbf{D})$ , and other symbols are conventional. For convenience, the terms  $-\nabla \cdot Q_K^\varpi$ ,  $-\nabla \cdot Q_A^\varpi$ ,  $-\nabla_h \cdot Q_p^\varpi$ , and  $-\nabla_z \cdot Q_p^\varpi$  are written as  $\Delta Q_K^\varpi$ ,  $\Delta Q_A^\varpi$ ,  $\Delta_h Q_p^\varpi$ , and  $\Delta_z Q_p^\varpi$ , respectively. Note that the sum of all cross-scale transfer processes  $\Gamma^\varpi$  is zero, without energy generation or loss as a whole, described as follows:

$$\sum_{\varpi} \sum_n \Gamma_n^\varpi = 0, \quad (6)$$

where summations  $\sum_{\varpi}$  and  $\sum_n$  involve all scale windows  $\varpi$  and sampling time steps, respectively. This property, which is

not satisfied in classic energetics formalism, is in accurate alignment with the principles of the conventional instability theory (Liang and Robinson 2007); thus,  $\Gamma$  is termed “canonical transfer” for distinction (Liang 2016). The canonical transfers ( $\Gamma^\varpi$  terms) in Eqs. (4) and (5) must be further decomposed via “interaction analysis” (Liang and Robinson 2005). The superscripts  $0 \rightarrow 1$  and  $2 \rightarrow 1$  are used to represent these window-to-window transfers. For instance,  $\Gamma_K^{0 \rightarrow 1}$  ( $\Gamma_A^{0 \rightarrow 1}$ ) denotes the conveyance of KE (APE) originating in the background flow window ( $\varpi = 0$ ) to the TRW window ( $\varpi = 1$ ), and a positive value of  $\Gamma_K^{0 \rightarrow 1}$  ( $\Gamma_A^{0 \rightarrow 1}$ ) indicates a forward energy cascade via barotropic (baroclinic) instability (Liang and Robinson 2007). Likewise,  $\Gamma_K^{2 \rightarrow 1}$  ( $\Gamma_A^{2 \rightarrow 1}$ ) denotes the scale interaction between  $\varpi = 2$  and  $\varpi = 1$ , with a positive value indicating an inverse cascade of KE (APE). In this study, our primary emphasis is on energetics within window  $\varpi = 1$ , which corresponds to the observed typical period of deep current variability.

### 3. Results

#### a. 10–20-day deep-current variability

The most significant characteristics of the observed deep currents were the dominant period in the 10–20-day intraseasonal frequency band and the occurrence of spectral peaks on 11 days in both directions (Fig. 2). Based on spectral analysis, the raw data were 10–20-day bandpass filtered to extract deep oscillations. To assess the influence of these oscillations on the overall variability of bottom subtidal currents, we presented the 10–20-day bandpass-filtered and the 3-day low-pass-filtered velocities in Fig. 3 and calculated the ratios of their standard deviations (STD). Both the ratios of the velocity components were above 50%, indicating that the 10–20-day fluctuations accounted for more than 50% of the overall variability of subtidal deep currents. Of note, the STD of 10–20-day  $v$  ( $3.02 \text{ cm s}^{-1}$ ) was 2 times that of  $u$  ( $1.50 \text{ cm s}^{-1}$ ), implying that the fluctuations were stronger in the cross-slope direction. The maximum amplitude of the 10–20-day oscillations was  $10.71 \text{ cm s}^{-1}$  ( $5.63 \text{ cm s}^{-1}$ ) in the cross-slope (along-slope) direction.

#### b. Dynamics for TRWs in low-latitude region

Energetic deep-current variability in a complex topography is associated with TRWs in many cases (e.g., Hamilton 2009; Wang et al. 2021; Shu et al. 2022). Beginning with the linear, hydrostatic, and Boussinesq equations, the governing equation for TRWs can be expressed in Cartesian coordinates as follows:

$$\frac{\partial}{\partial t} \left[ p_{xx} + p_{yy} + \frac{1}{N^2} \left( \frac{\partial^2}{\partial t^2} + f_0^2 \right) p_{zz} \right] + \beta p_x = 0. \quad (7)$$

Assuming time dependence of  $e^{-i\omega t}$ , Eq. (7) can be revised as follows:

$$\frac{\partial}{\partial t} \left[ p_{xx} + p_{yy} + \frac{f_0^2 - \omega^2}{N^2} p_{zz} \right] + \beta p_x = 0. \quad (8)$$

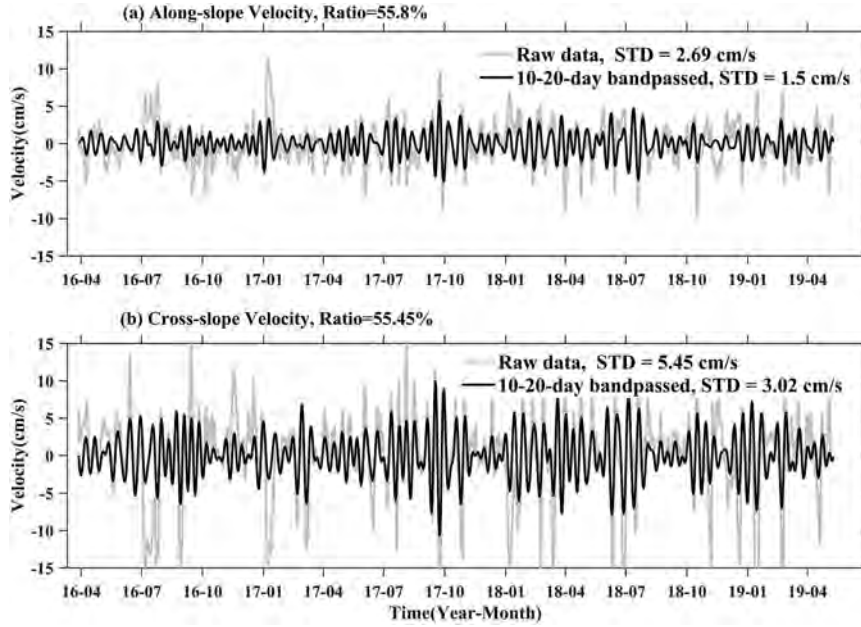


FIG. 3. Observed 3-day low-pass filtered and 10–20-day filtered bottom (a)  $u$  and (b)  $v$  at mooring Q3. Gray and black lines indicate the 3-day low-pass and 10–20-day filtered velocities, respectively. The title of each panel displays the ratio between the STD of 10–20-day bandpassed velocities and the STD of 3-day low-pass filtered velocities.

The boundary conditions consist of a rigid lid and no normal flow through the bottom; that is,

$$\frac{\partial}{\partial t} p_z = 0, \quad \text{at } z = 0, \quad (9)$$

$$\frac{\partial}{\partial t} p_z = \frac{N^2}{f_0} (p_x h_y - p_y h_x), \quad \text{at } z = -h, \quad (10)$$

where  $h$  represents the water depth,  $f_0$  indicates the local Coriolis parameter, and  $(h_x, h_y)$  is the horizontal gradient of the topography. Substituting the solution of the form

$$p = A(z)e^{i(kx+ly-\omega t)} \quad (11)$$

into (8) and the boundary conditions (9) and (10), we obtain

$$A(z) = A_0 \cosh(\lambda z), \quad (12)$$

$$\lambda^2 = \left( k^2 + l^2 + \frac{\beta k}{\omega} \right) \left( \frac{N^2}{f_0^2 - \omega^2} \right), \quad (13)$$

$$\omega = \frac{N^2}{f_0 \lambda \tanh(\lambda h)} (k h_y - l h_x), \quad (14)$$

where  $A_0$  is a constant and  $1/\lambda$  represents the TRW vertical trapping scale. Substituting Eq. (13) into Eq. (14), we obtain TRW dispersion relation that considers the smaller Coriolis parameter  $f_0$  and stronger  $\beta$  effect in the subtropical region, as follows:

$$\begin{aligned} \omega &= \frac{N \left( \frac{k}{K_l} h_y - \frac{l}{K_l} h_x \right) \sqrt{f_0^2 - \omega^2}}{f_0 \tanh(\lambda h) \sqrt{1 + \frac{\beta k}{\omega K_l^2}}} = \frac{N (\mathbf{K}_l \times \nabla h \cdot \mathbf{z}) \sqrt{f_0^2 - \omega^2}}{f_0 K_l \tanh(\lambda h) \sqrt{1 + \frac{\beta k}{\omega K_l^2}}} \\ &= \frac{N |\nabla h| \sin \theta \sqrt{1 - \frac{\omega^2}{f_0^2}}}{\tanh(\lambda h) \sqrt{1 + \frac{\beta k}{\omega K_l^2}}}, \end{aligned} \quad (15)$$

where  $\mathbf{K}_l = (k, l)$  is the horizontal wavenumber vector,  $K_l = \sqrt{k^2 + l^2}$  is the magnitude of  $\mathbf{K}_l$ ,  $\mathbf{z}$  is the unit vector along the  $z$  axis,  $K_l \times \nabla h \cdot \mathbf{z}$  represents the  $z$  component of  $K_l \times \nabla h$ , and  $\theta$  indicates the clockwise angle that  $\mathbf{K}_l$  forms with cross-isobathic downslope direction  $\text{Dir}(\nabla h)$ , satisfying  $\theta = \text{Dir}(\nabla h) - \text{Dir}(K_l)$ . In Eq. (15), all terms must be greater than zero except  $(K_l \times \nabla h \cdot \mathbf{z})$  and  $f_0$ . To keep  $\omega$  positive, the sign of  $K_l \times \nabla h \cdot \mathbf{z}$  should be the same as that of  $f_0$ . Therefore, the direction of the wavenumber vector points to the right (left) of the downslope direction, indicating that TRWs propagate with deep water on its left (right) in the Northern (Southern) Hemisphere.

If the motion is low frequency [i.e.,  $(f_0^2/\omega^2) > 10$ ] and the topographic  $\beta$  effect ( $\beta_{\text{Topo}}$ ) is dominant [i.e.,  $\beta_{\text{Topo}} = (f_0 |\nabla h|/h) > 10\beta$ ], both  $\sqrt{1 + [\beta k/(\omega K_l^2)]}$  (term I) and  $\sqrt{1 - (\omega^2/f_0^2)}$  (term II) are approximately 1; then [with  $\tanh(\lambda h) = 1$ ], Eq. (15) is simplified as  $\omega = N |\nabla h| \sin \theta$ , which was commonly used in previous studies in the SCS and GoM

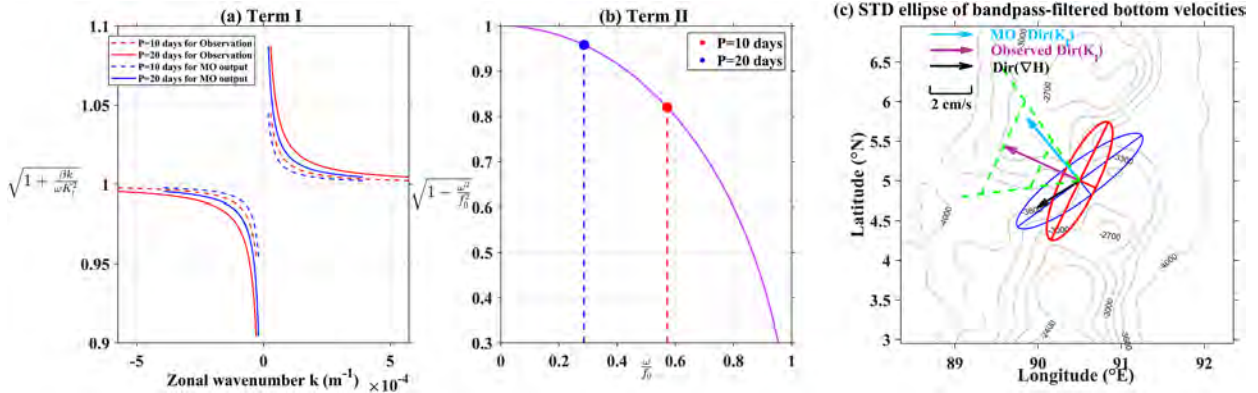


FIG. 4. Topographic Rossby wave dispersion elements. (a) Term I  $\{\sqrt{1 + [\beta k/(\omega K_l^2)]}\}$  for varying zonal wavenumber and (b) term II  $[\sqrt{1 - (\omega^2/f_0^2)}]$  for varying frequency. (c) STD ellipse of 10–20-day filtered bottom currents. The red and blue ellipses were derived from the 10–20-day filtered velocities obtained from observation and model output. The  $\text{Dir}(K_l)$  of the observation and MO model output was derived from the minor axis of their STD ellipse and represented by purple and blue arrows, respectively. The theoretical range of  $\text{Dir}(K_l)$  derived from the TRW theory was indicated by the green dashed line domain.

(e.g., Oey and Lee 2002; Shu et al. 2016). However, in our case, these conditions could not be satisfied. Considering the dominant period of motion to be within 10–20-day period band ( $\omega$  is within  $3.64\text{--}7.27 \times 10^{-6} \text{ s}^{-1}$ ),  $f_0 = 12.7 \times 10^{-6} \text{ s}^{-1}$ ,  $|\nabla h| \sim 0.01$ , and  $h \sim 3000 \text{ m}$ , then the value of  $f_0^2/\omega^2$  is within 3.1–12.2 and  $\beta_{\text{Topo}} \approx 2\beta$ ; in other words, the  $\omega^2/f_0^2$  and  $\beta$  terms in Eq. (15) cannot be ignored. This is not surprising because the mooring is located at  $5^\circ\text{N}$ , resulting in a much smaller  $f_0$  and a stronger  $\beta$  effect. Previous studies suggested that the 10–20-day TRWs satisfy the short-wavelength assumption based on their observations (e.g., Shu et al. 2016, 2022; Q. Wang et al. 2019; Wang et al. 2021), which assumes a wavelength  $L < 200 \text{ km}$  (Hamilton 2009). For the short waves with a period of 10–20 days, we could infer that  $K_l = 2\pi/L > 2\pi/200000 \text{ m}^{-1} = 3.14 \times 10^{-5} \text{ m}^{-1}$  and zonal wavenumber  $k = K_l \cos 154.30^\circ < -2.8 \times 10^{-5} \text{ m}^{-1}$ , then values of  $\sqrt{1 + [\beta k/(\omega K_l^2)]}$  (term I) exceeded 0.9 and that of  $\sqrt{1 - (\omega^2/f_0^2)}$  (term II) ranged from 0.82 to 0.96 (Figs. 4a,b). Therefore, the ratio of term I and term II (i.e., term I/term II) was within 0.94–1.22, thus

$$\lambda = \frac{NK_l}{f_0} \frac{\sqrt{1 + \frac{\beta k}{\omega K_l^2}}}{\sqrt{1 - \frac{\omega^2}{f_0^2}}} = \frac{NK_l}{f_0} \frac{\text{term I}}{\text{term II}} > 0.0019,$$

and  $\tanh(\lambda h \geq 5.78) = 1$ , indicating  $\tanh(\lambda h) = 1$  is valid under the short-wavelength assumption. It should be noted that the group velocity  $\mathbf{C}_g = (\partial\omega/\partial k, \partial\omega/\partial l)$  is not perpendicular to the wave vector if the  $\beta k/(\omega K_l^2)$  of term I is kept in the TRW dispersion relation [i.e.,  $\omega = N|\nabla h| \sin\theta \sqrt{1 - (\omega^2/f_0^2)}/\sqrt{1 + [\beta k/(\omega K_l^2)]}$ ], but remains normal to  $\mathbf{K}_l$  if only  $\omega^2/f_0^2$  term is kept [i.e.,  $\omega = N|\nabla h| \sin\theta \sqrt{1 - (\omega^2/f_0^2)}$ ], mainly because  $\omega$  is dependent (independent) on the magnitude of  $K_l$  and  $\mathbf{K}_l \cdot \mathbf{C}_g = \mathbf{K}_l \cdot \nabla_{\mathbf{K}_l} \omega \neq 0 (=0)$  when the  $\beta k/(\omega K_l^2)$  of term I is kept (dropped) (Oey and Lee 2002).

To validate the observed 10–20-day fluctuations as TRWs, we compared the observed  $\text{Dir}(K_l)$  with the theoretical range of the wavenumber direction  $\text{Dir}(K_l)$  derived from the TRW dispersion relation. First, we calculated the STD ellipse of 10–20-day filtered currents to obtain the observed  $\text{Dir}(K_l)$ , which is represented by the minor axis direction of the STD ellipse (Hamilton 2009). To the north of the equator, TRWs propagate with deep water on their left, indicating the  $\theta$  is within  $(0, \pi/2)$  or  $(\pi/2, \pi)$  when  $\text{Dir}(K_l)$  points downslope or upslope (Oey and Lee 2002). In our case,  $\text{Dir}(\nabla h) = 213.10^\circ$ , observed  $\text{Dir}(K_l)$  was  $154.30^\circ$  and pointed downslope (purple arrow in Fig. 4c). With  $\tanh(\lambda h) = 1$ , two roots of  $\theta$  could be calculated from TRW dispersion relation [Eq. (16)], and its value should be within  $(0, \pi/2)$

$$\theta = \sin^{-1} \left[ \frac{\omega}{N|\nabla h|} \frac{\sqrt{1 + \frac{\beta k}{\omega K_l^2}}}{\sqrt{1 - \frac{\omega^2}{f_0^2}}} \right]. \quad (16)$$

Then, the theoretical  $\text{Dir}(K_l)$  can be expressed as follows:

$$\text{Dir}(K_l) = \text{Dir}(\nabla h) - \theta. \quad (17)$$

Given  $|\nabla h|$ ,  $N$ ,  $k$ ,  $K_l$ , and  $\omega$ , the theoretical range of  $\text{Dir}(K_l)$  could be derived from Eqs. (16) and (17). Considering that the  $\omega$  was within  $3.64\text{--}7.27 \times 10^{-6} \text{ s}^{-1}$  (i.e., a period of 10–20 days),  $\text{Dir}(K_l)$  pointed downslope, the environmental parameters  $|\nabla h| = 0.011$  and  $N = 7.8 \times 10^{-4} \text{ s}^{-1}$  at mooring Q3, we obtained the theoretical  $\theta$  ranging from  $24.83^\circ$  to  $90.00^\circ$ ; thus, theoretical  $\text{Dir}(K_l)$  was within  $(123.10^\circ, 188.27^\circ)$ , which was indicated by the green dashed line domain in Fig. 4c. In other words, the energetic 10–20-day fluctuations at Q3 could be considered as TRWs due to the observed  $\text{Dir}(K_l)$  closely conforming to the dispersion relation of 10–20-day TRWs.

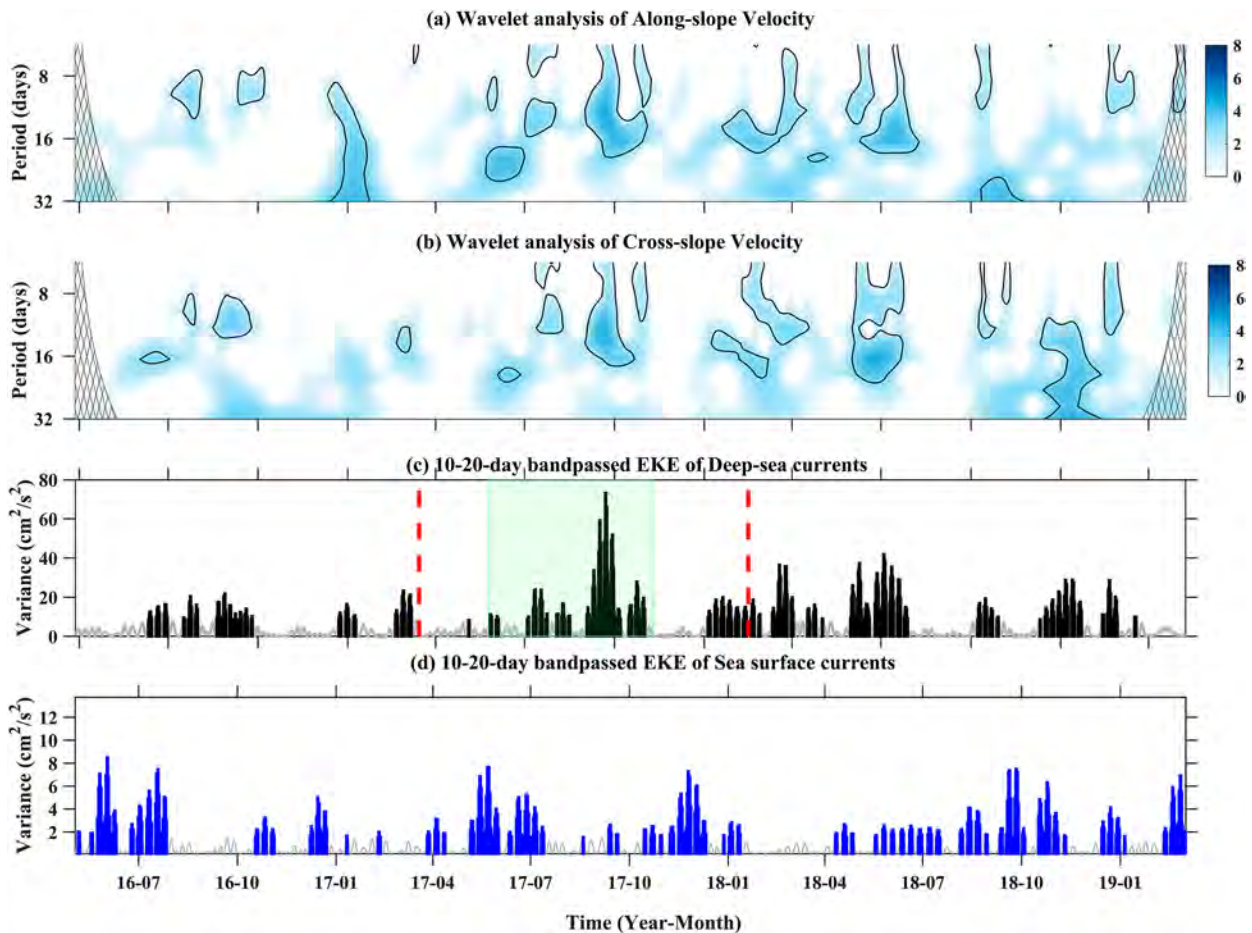


FIG. 5. (a) Wavelet power spectrum of observed bottom along-isobathic and (b) cross-isobathic velocities at mooring Q3. The 95% confidence level is indicated by the black contours. (c) The 10–20-day filtered bottom and (d) surface EKEs, calculated from the 10–20-day filtered velocities and AVISO dataset, respectively. EKEs exceeding their STDs are highlighted in black and blue, respectively. Red dashed lines indicate the start and end times of upper-layer observations. Green shading represents the energetic period of bottom TRWs selected for further analysis.

### c. Association between the 10–20-day oscillations of deep currents and upper-ocean processes

To identify the burst period of energetic TRWs, we employed wavelet analysis to the raw velocity data (i.e.,  $u$  and  $v$ ), and the 10–20-day eddy kinetic energy (EKE) was calculated using bandpass-filtered data. The significantly enhanced period of the deep 10–20-day oscillations was similar in both directions (Figs. 5a,b) and coincident with the intensification of the 10–20-day EKE (Fig. 5c). Previous studies have suggested that TRWs may be generated by upper-layer mesoscale oscillations, such as upper-layer eddies (Ma et al. 2019; Shu et al. 2022; Wang et al. 2021). The 10–20-day surface EKE was obtained from the 10–20-day filtered geostrophic velocities from the AVISO dataset to illustrate the intensity of surface eddies. Here, we assumed that the EKEs of the energetic bottom TRW and upper-layer eddy are larger than their STDs (marked in black and blue bars in Figs. 5c,d, respectively). Evidently, upper-layer eddies do not appear to be related to the occurrence of strong bottom TRWs.

To understand the association between the 10–20-day oscillations of deep currents and other upper-layer processes, velocity data over 39–948 m derived from the ADCPs were used. The 10–20-day oscillations of cross-slope currents were more energetic below 500 m than those near the surface, while the 10–20-day oscillations of along-slope currents were mostly present above 300 m and decreased in strength with increasing depth (Figs. 6a,b). Subsequently, we used this frequency band to extract signals in the upper ocean and applied correlation analysis to the 10–20-day upper and deep oscillations in both directions. In the along-slope direction, the correlation between the upper and bottom oscillations was weak, with most correlation coefficients being  $<0.2$  and below the 95% confidence level (gray line in Fig. 6c). In contrast, almost all correlation coefficients below 300 m in the cross-slope direction were larger than 0.2 and exceeded the 95% confidence level, indicating a strong association between deep 10–20-day variability and cross-slope subthermocline (300–950 m) oscillations (Fig. 6d).

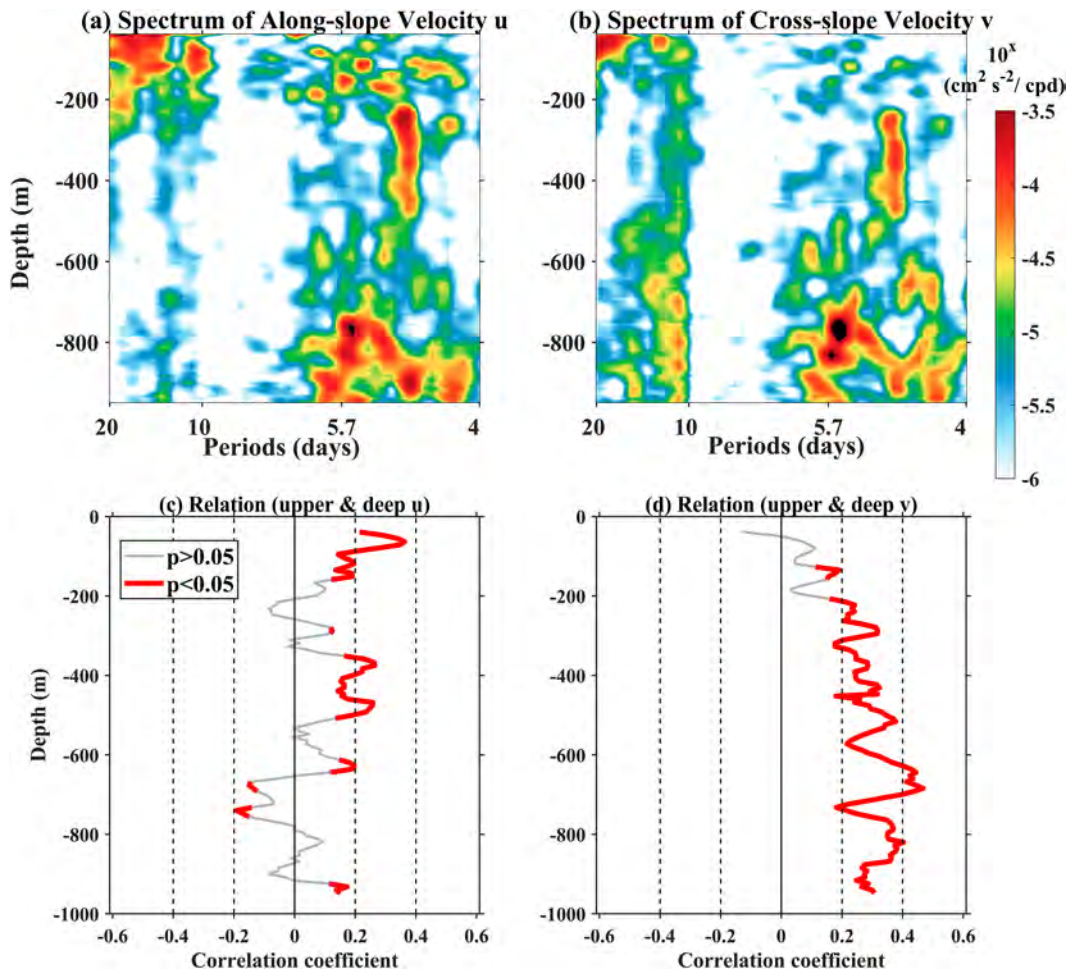


FIG. 6. Power spectrum of the observed upper (a)  $u$  and (b)  $v$  by mooring Q3. (c) Correlation coefficients between upper velocities at different depths and deep velocities in along-isobathic and (d) cross-isobathic directions, respectively. In (c) and (d), coefficients exceeding the 95% confidence level based on the Student's  $t$  test are plotted in red.

To further understand the dynamics between upper-layer and deep-sea flows, we employed the empirical orthogonal function (i.e., EOF) analysis to the subthermocline raw velocities over 300–950 m during the energetic TRW period (from 25 May to 10 November 2017, 170 days; green shading in Fig. 5c). The first, second, and third modes (i.e., EOF1, EOF2, and EOF3) contributed to over 80% of the total variance (Figs. 7a,b). Next, we calculated the power spectra of the principal components (PCs) of the first and second modes to reveal the general pattern of subthermocline flows. Spectral peaks in the 10–20-day period were detected in the first PC (PC1) alone in both directions, while the spectral power of cross-isobathic flows was relatively strong in the period band of 10–20 days (Figs. 7c–f). Therefore, we calculated the lag correlation coefficients between the 10–20-day bandpass-filtered PCs and deep flows (Fig. 8). The most significant correlation was at zero lag (3 days) in the cross- (along-) slope direction (Figs. 8a,b), indicating coupling between cross-slope subthermocline and deep motions. Since TRWs are generated

by cross-isobathic motions as water columns are compressed and stretched over a sloping topography (Oey and Lee 2002), we hypothesized that subthermocline cross-slope motions induced deep cross-isobathic motions through the barotropic mode (i.e., EOF1), providing the necessary conditions for TRWs generation.

Figure 9 showed the 10–20-day filtered velocity profiles and depth-averaged (300–950 m) subthermocline velocities. The energetic periods of the subthermocline (black bars; Figs. 9c,d) and deep (red bars; Figs. 9c,d) motions were defined as absolute values larger than their STDs. A clear vertical coupling structure was noted in the  $v$  components, whose energetic period was from late May to early November 2017 in both subthermocline and deep ocean (Fig. 9d). As subthermocline  $v$  increased in June 2017, deep  $v$  was strengthened subsequently and tended to be in the same phase as in the upper flows, consistent with the feature of the barotropic mode (Fig. 9d). When the water column was compressed or stretched, the TRWs burst due to potential vorticity conservation.



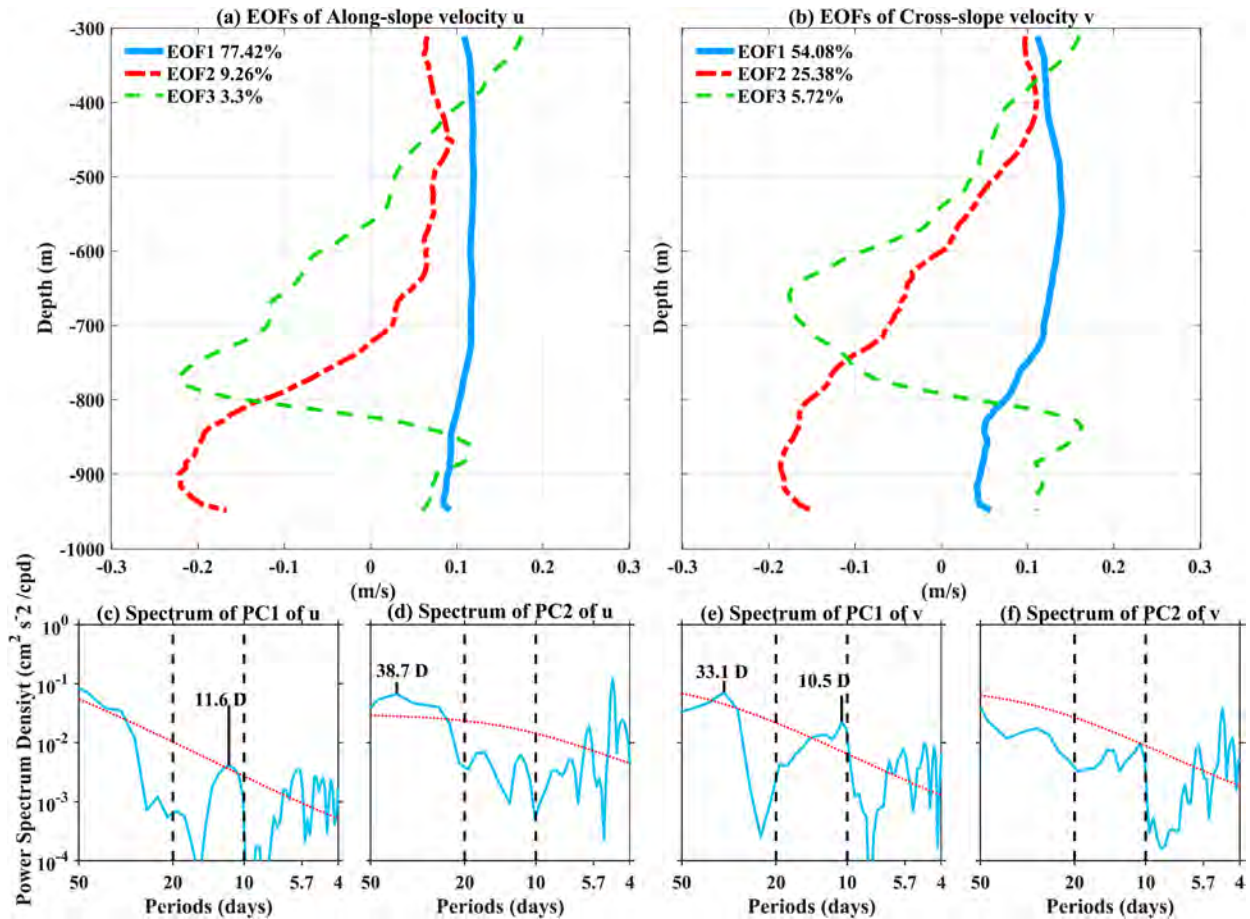


FIG. 7. First three modes of EOF decomposition of the observed upper (a)  $u$  and (b)  $v$  between 300 and 950 m. Power spectrum analysis of the (c) PC1 and (d) PC2 of upper-ocean  $u$  between 300 and 950 m. Power spectrum analysis of the (e) PC1 and (f) PC2 of upper-ocean  $v$  between 300 and 950 m. The 95% confidence level test against red noise was indicated by the dotted red lines in (c)–(f).

**4. Discussion**

Although the above analysis showed that the 10–20-day deep-sea TRWs were dynamically linked to subthermocline oscillations, detailed energetics and energy transfer dynamics of this deep-sea variability remained unknown. Mooring observation is limited to a single location and may not capture the full extent of the underlying energetics. Therefore, we used the MO model output to analyze the energetics of TRWs. The prerequisite of using model output is that the model can reproduce the observed TRWs. First, we compared the power spectrum and the STD ellipse between model output and observation. The result showed that there were significant 10–20-day oscillations in the bottom velocities derived from model output (blue solid line; Fig. 2). The magnitude of the STD ellipse calculated from model output was similar to that calculated from observation, despite the wavenumber direction ( $128.65^\circ$ ; blue arrow in Fig. 4c) being different from the observed value ( $154.30^\circ$ ), which might result from the uncertainty of environmental parameters [e.g.,  $|\nabla h|$  and  $\text{Dir}(\nabla h)$ ] and smoothing scale of topography in the model. Second, we examined if the 10–20-day oscillations in the MO model

satisfy the TRW dispersion relation. It was obvious that the  $\text{Dir}(K_l)$  obtained from the MO model (blue arrow in Fig. 4c) was within the theoretical range, suggesting that the 10–20-day oscillations in the MO model also satisfy the TRW dynamic. In other words, the discrepancy of  $\text{Dir}(K_l)$  between observation and MO was acceptable in TRW theory. Third, as the study specifically focused on the energetics of oscillations in the 10–20-day period band, we compared the burst of the 10–20-day EKEs between the observation and MO model output in Fig. 10 (values smaller than their STDs are not shown in Figs. 10b,d). Both the 10–20-day upper-layer and bottom EKEs from the model output had similar enhancement time periods to that of the observations (Fig. 10). Moreover, the amplitude of upper-ocean and bottom EKE from model output was comparable to that of observation, that is to say, the model accurately simulated the timing, generation, and intensity of 10–20-day oscillations throughout the observation period. In other words, the MO model output could reproduce 10–20-day oscillations and associated generation processes, indicating its usefulness in exploring deep-sea energetics and energy transfer from the upper to deep ocean.

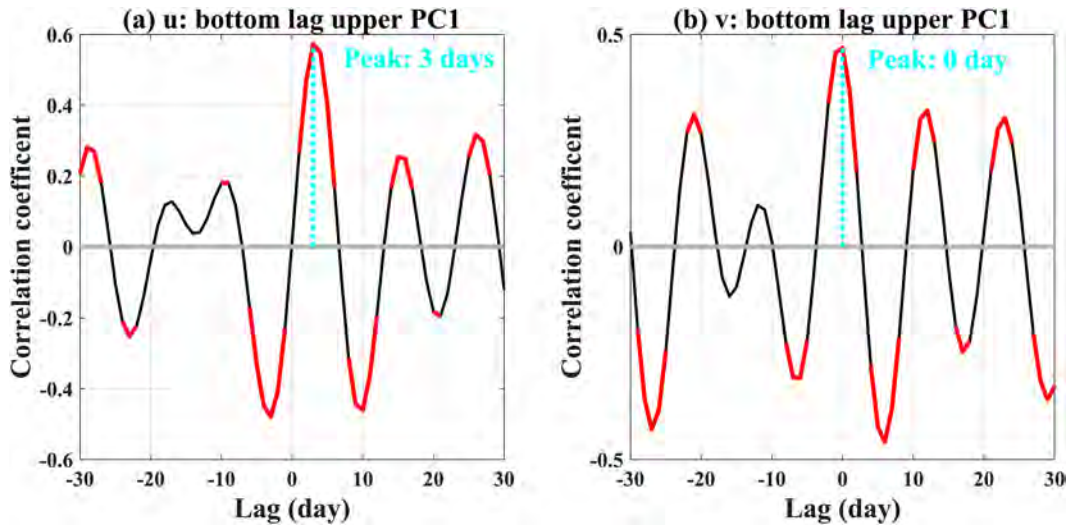


FIG. 8. Time-lag correlations. (a) Lag correlation between the bottom  $u$  and PC1 of upper  $u$ . (b) Lag correlation between the bottom  $v$  and PC1 of upper  $v$ . Coefficients over the 95% significance level based on Student's  $t$  test are indicated in red.

To better understand the energetics at mooring Q3, we employed MS-EVA (Liang 2016) on the MO model output. Since the window bounds and length of the time series were exponential functions of base 2 for MS-EVA, we selected a window of 8–16 days to extract the energy of TRWs, and the data ranged from 1 January 2014 to 10 August 2019 (2048 days). It should be noted that  $APE^1$  was one order smaller than  $K^1$  near

the bottom (Figs. 11a,b). Moreover, except  $b^1$ , which appeared in both Eqs. (4) and (5), the other terms in Eq. (5) were much less than  $\Delta_z Q_p^1$  and  $\Delta_y Q_p^1$  in Eq. (4) (not shown here). Therefore, we will not analyze the result of Eq. (5).

The deep-layer  $K^1$  burst with a bottom-intensified characteristic, which was consistent with the TRW feature (Fig. 11a). Among the terms of the  $K^1$  budget [Eq. (4)], the horizontal

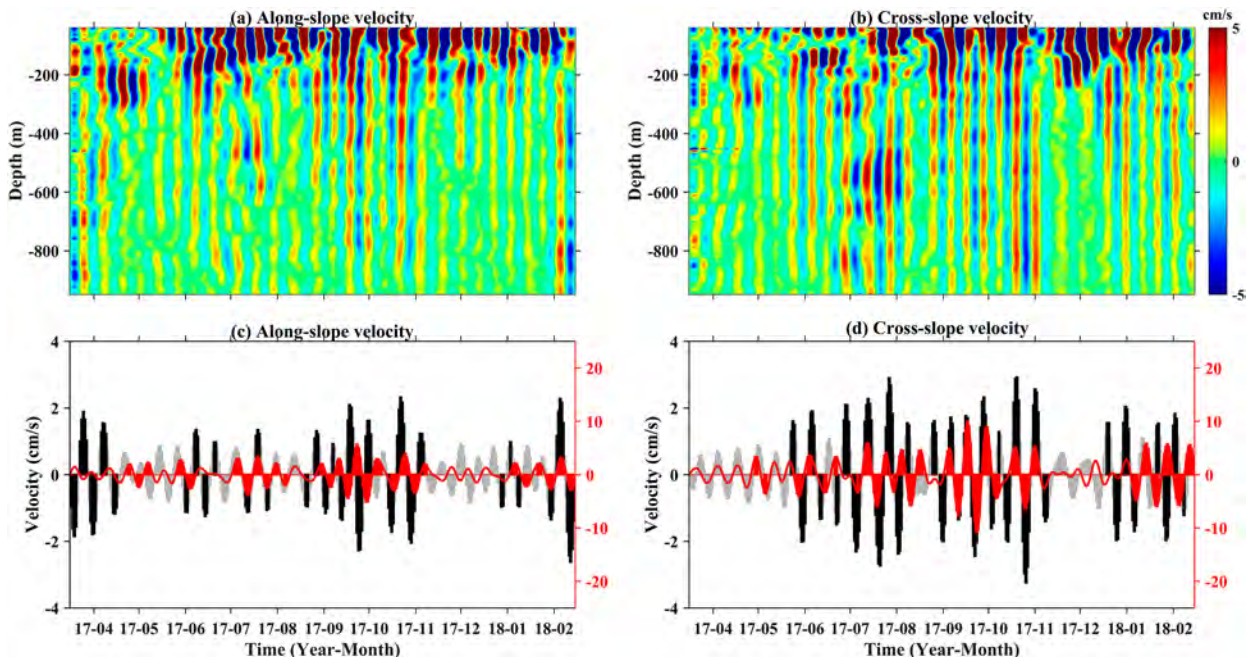


FIG. 9. Observed upper and bottom velocities at mooring Q3. (a) Profiles of 10–20-day bandpass-filtered  $u$  and (b)  $v$  in the upper layer. The 10–20-day filtered upper velocities averaged from 300 to 950 m (gray bars) and bottom velocities (red lines) in (c) along-isobathic and (d) cross-isobathic directions. In (c) and (d), the upper averaged and bottom velocities exceeding their STDs are plotted in black and red bars, respectively.

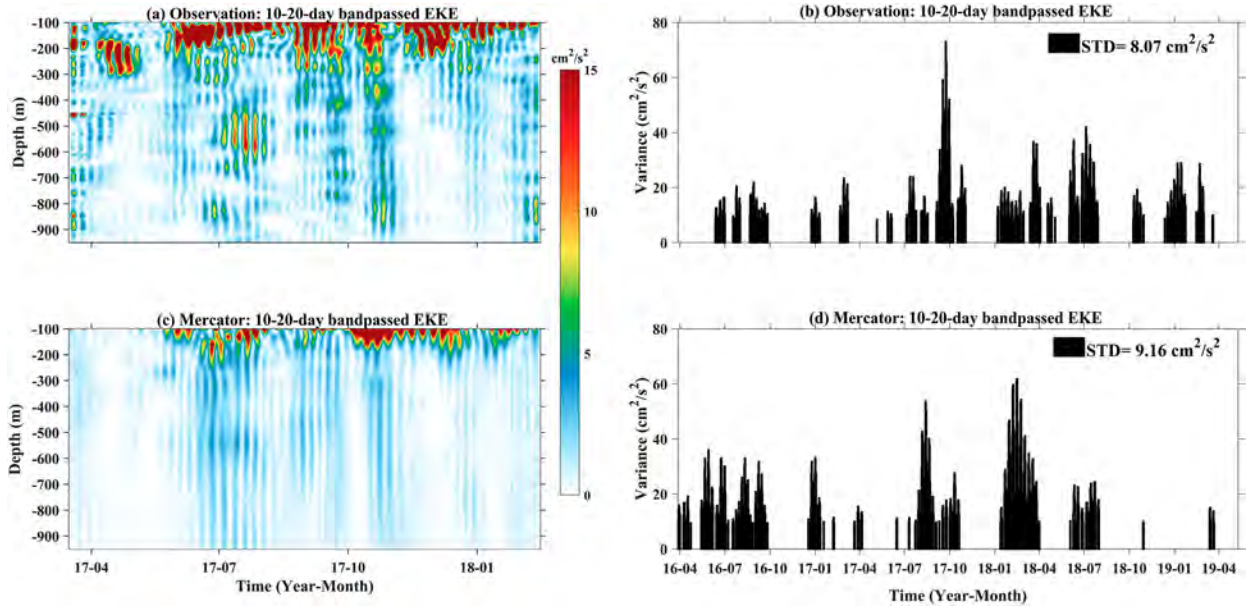


FIG. 10. (a) The 10–20-day filtered upper-layer (100–950 m) and (b) bottom EKE obtained from observational data at mooring Q3. (c),(d) The corresponding results from Mercator Ocean model output. EKEs were derived from the 10–20-day bandpass-filtered velocities. In (b) and (d), only values exceeding their STDs are shown.

and vertical pressure work ( $\Delta_h Q_p^1$  and  $\Delta_z Q_p^1$ ) were relatively larger than the other terms (Fig. 11). The positive vertical pressure work  $\Delta_z Q_p^1$  indicated that  $K^1$  was transported downward from the upper ocean. The negative horizontal pressure work  $\Delta_h Q_p^1$  implied that  $K^1$  was horizontally redistributed by

the horizontal pressure gradient and acted as a sink for the  $K^1$  reservoir. We noticed that almost each burst of  $K^1$  robustly corresponded to an enhanced positive  $\Delta_z Q_p^1$  value (negative  $\Delta_h Q_p^1$  value) from 2014 to 2019, indicating that  $\Delta_z Q_p^1$  ( $\Delta_h Q_p^1$ ) typically served as the dominant energy source (sink) for

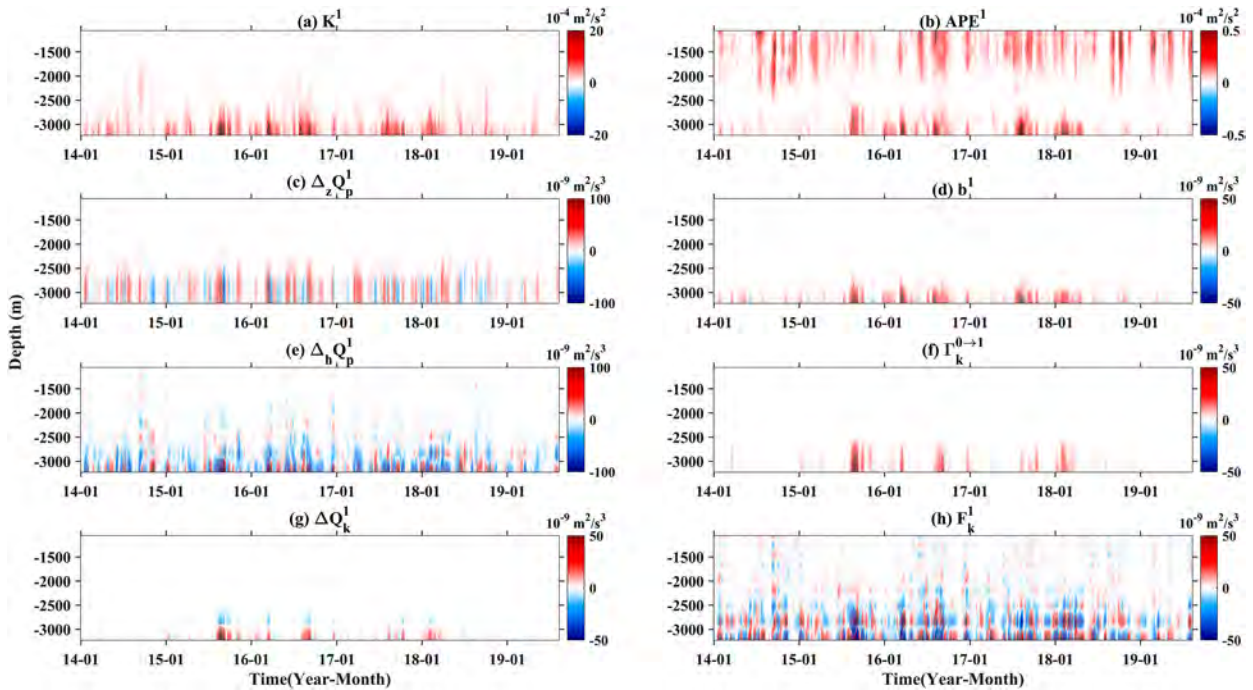


FIG. 11. Profiles of the energy reservoir and energetics terms (a)  $K^1$ , (b)  $APE^1$ , (c)  $\Delta_z Q_p^1$ , (d)  $b^1$ , (e)  $\Delta_h Q_p^1$ , (f)  $\Gamma_k^{0 \rightarrow 1}$ , (g)  $\Delta Q_k^1$ , and (h)  $F_k^1$ . The other terms are negligible and not shown.

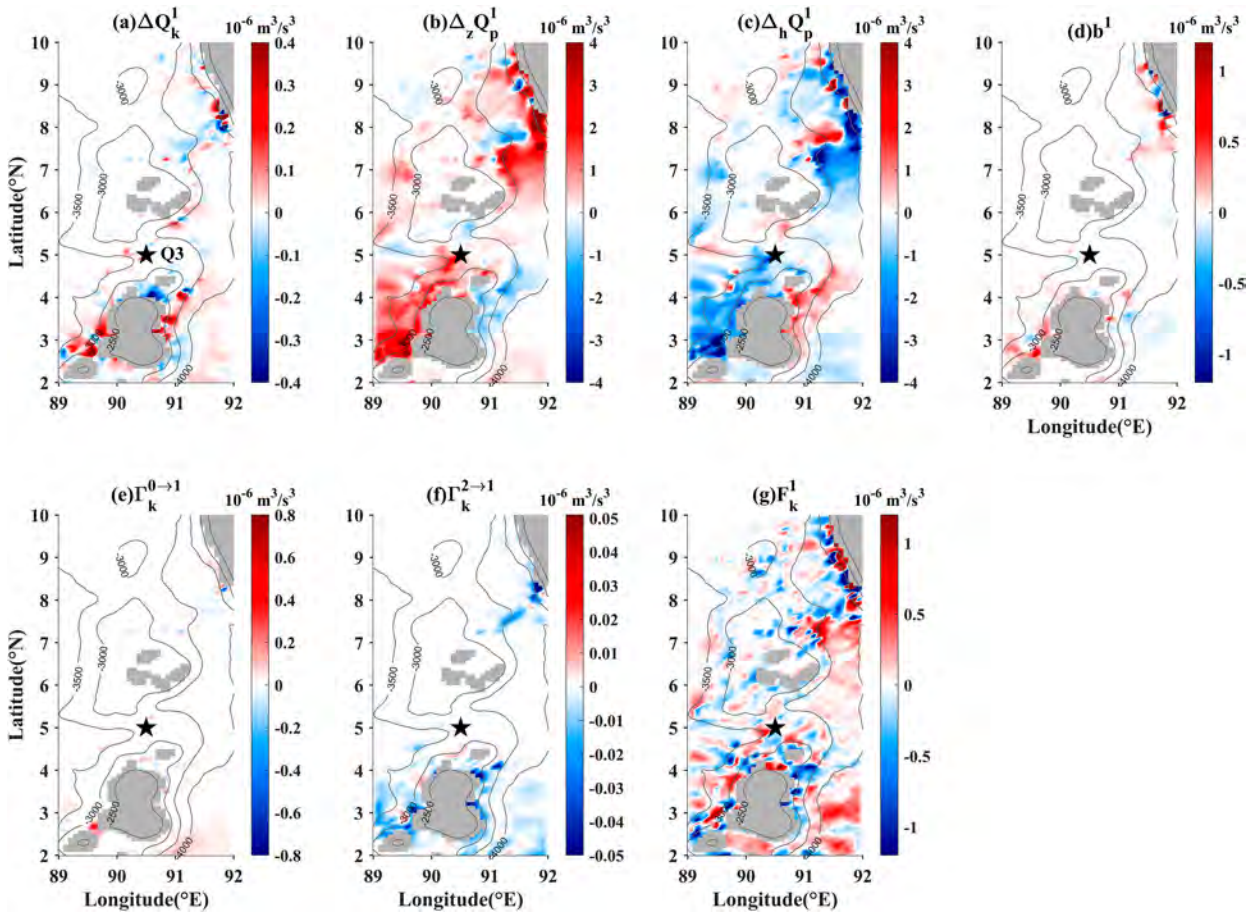


FIG. 12. Horizontal maps of the energetic terms (a)  $\Delta Q_K^1$ , (b)  $\Delta_z Q_p^1$ , (c)  $\Delta_h Q_p^1$ , (d)  $b^1$ , (e)  $\Gamma_K^{0 \rightarrow 1}$ , (f)  $\Gamma_K^{2 \rightarrow 1}$ , and (g)  $F_K^1$  vertically integrated from 2000 m to the bottom. The black star indicates the location of mooring Q3. The grids without data are masked with gray shading. The black contours indicate the  $-2500$ ,  $-3000$ ,  $-3500$ , and  $-4000$  m isobaths.

bottom TRWs (Figs. 11a,c,e). As described by Quan et al. (2021a), the mesoscale perturbations from the upper ocean can transport energy to deep oscillations via deforming the isopycnals to do work (i.e., vertical pressure work  $\Delta_z Q_p^1$ ). This vertical process can explain the vertical linkage between the upper-layer and deep-sea current variability from an energetics aspect, which is reported in the Kuroshio Extension region (Yang et al. 2021). The buoyancy conversion  $b^1$  signals were weaker in the interior ocean but stronger beneath the water depth of  $\sim 3000$  m and showed a bottom-intensified distribution (Fig. 11d). From this result, APE<sup>1</sup> could be converted to  $K^1$ , thus favoring TRW generation in the deep ocean. In addition, the canonical transfer  $\Gamma_K^{0 \rightarrow 1}$  and advection of KE  $\Delta Q_K^1$  also showed overwhelmingly positive and bottom-intensified patterns in the deep layer, with their positive timing corresponding to some strong  $K^1$  events (Figs. 11f,g). Note that the positive  $\Delta Q_K^1$  might imply the effect of TRW propagation from upstream, the result suggested that energetic bottom TRWs can gain energy locally through the release of background-flow KE via barotropic instability and non-locally through advective transport of  $K^1$  (possibly via TRWs propagation), which is coincident with the mechanisms

revealed by Ma et al. (2019) and Quan et al. (2021b). The residual term  $F_K^1$  showed alternating positive and negative signals (Fig. 11h), while its time- and depth-averaged value was negative (Fig. 13a), indicating part of  $K^1$  might be dissipated by bottom friction.

To explore the universal dynamics in the seamount region ( $2^\circ$ – $10^\circ$ N,  $89^\circ$ – $92^\circ$ E), we time averaged the  $\sim 6$ -yr variables in the  $K^1$  budget equation and integrated from 2000 m to the bottom (Fig. 12). Over the long-term perspective, pressure work significantly dominated the  $K^1$  budget in comparison to other terms, by at least 3 times the other terms. In the sub-equatorial region, the vertical pressure work  $\Delta_z Q_p^1$  was mainly positive, while the horizontal pressure work  $\Delta_h Q_p^1$  was mainly negative, and both peaked in the region southwest of Q3. This area also exhibited positive values for the advection term  $\Delta Q_K^1$  and buoyancy conversion  $b^1$ , as shown in Figs. 12a–d. These distribution patterns of the pressure work highlighted an energy pathway in the subequatorial deep layer (i.e., from 2000 m to bottom); as such, deep fluctuations were energized by energy transport from the upper ocean and radiated by horizontal pressure work process, and these processes were widespread and frequent in the seamount region.

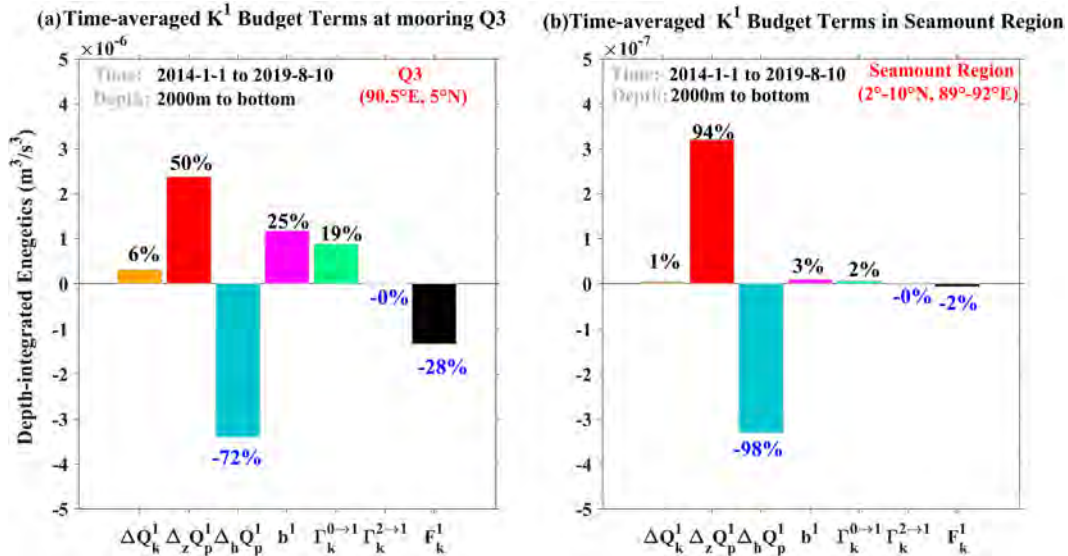


FIG. 13. Time-averaged (from 1 Jan 2014 to 10 Aug 2019, 2048 days)  $K^1$  budget terms vertically integrated from 2000 m to the bottom. Results (a) at mooring Q3 and (b) area averaged over the seamount region ( $2^\circ$ – $10^\circ$ N,  $89^\circ$ – $92^\circ$ E).

To quantify the contribution of each  $K^1$  budget term in the deep layer, depth-integrated variables in the entire seamount region were area averaged and then the ratios of these variables and the total  $K^1$  source were calculated, as shown in Fig. 13. At Q3, the vertical pressure work  $\Delta_z Q_p^1$  was the dominant energy source for  $K^1$ , accounting for approximately 50% of the total  $K^1$  sources (Fig. 13a). The buoyancy conversion  $b^1$  played a secondary role in TRW generation (contributing to ~25% of the total  $K^1$  sources), whereas the contribution of canonical transfer  $\Gamma_k^{0 \rightarrow 1}$  (~19%) and advective transport of KE  $\Delta Q_k^1$  (~6%) to the total  $K^1$  sources were less. The horizontal pressure work  $\Delta_b Q_p^1$  was the primary mechanism that radiated  $K^1$  (contributing to ~72% of the total  $K^1$  sinks), while the residual term  $F_k^1$  was the secondary mechanism that dissipated  $K^1$  and contributed to ~28% of the sinks. Furthermore, the results for the entire seamount region confirmed that the vertical (horizontal) pressure work played a vital role in the generation (redistribution) of deep-layer  $K^1$  energy, accounting for 94% (98%) of the total  $K^1$  sources (sinks), consistent with the pattern in the southwest of Q3 (Figs. 12b,c and 13b). Although advective transport and buoyancy conversion were favorable for  $K^1$  generation in specific areas (e.g., southwest of Q3), their contributions were limited when averaged in the seamount region (Fig. 13).

Overall, these results suggested upper-layer perturbations were the energy source of deep current variability on window  $\varpi = 1$ , transporting energy into the deep ocean via vertical pressure work. The deep TRWs were triggered by the 10–20-day perturbations in subthermocline. The spectrum of observed velocities between 300 and 950 m showed that the signals with the 10–20-day periods were more energetic in the meridional direction than that in the zonal direction (not shown here). Such characteristics of the oscillations are similar to 10–20-day Yanai waves (also as mixed Rossby–gravity waves), which show a

quasi-biweekly meridional variability generated by wind forcing or current instabilities in the equatorial Indian Ocean (Schott et al. 1994; Sengupta et al. 2004; Chatterjee et al. 2013; Arzeno et al. 2020). In the equatorial region south of Q3 (i.e., on the equator at  $90^\circ$ E), 10–20-day Yanai waves were observed by Masumoto et al. (2005), with signals mainly confined within the upper 100 m. In contrast, the observed 10–20-day meridional oscillations at Q3 were weak near the surface but energetic in the subthermocline, indicating that they were not generated locally but possibly originated from remote forcing. Therefore, we hypothesize that the subthermocline 10–20-day meridional oscillations are equatorial Yanai waves propagating downward and may still exhibit considerable strength near  $5^\circ$ N (e.g., Chatterjee et al. 2013), similar to the semiannual variability at the middepth (~1200 m) of Q3 caused by the boundary-reflected downward-propagating Rossby waves (Huang et al. 2019). Note that we could not obtain the vertical trapping scale ( $h_{\text{trap}} = 1/\lambda$ ) of TRWs from the bottom observation at a single depth. The vertical trapping scale  $1/\lambda$  of TRWs can be estimated by the ratio of KE (Ratio<sub>KE</sub>) between the two layers (e.g.,  $z_1$  and  $z_2$ ) following  $\text{Ratio}_{KE} = [\cosh(\lambda z_2)/\cosh(\lambda z_1)]^2$  (Hogg 2000; Thompson and Luyten 1976). Based on the model output,  $z_1 = 2866$  m,  $z_2 = 3220$  m,  $\lambda = 0.0022$ , thus  $h_{\text{trap}} = 1/\lambda \approx 456$  m, the averaged  $K_l = (f/Nh_{\text{trap}})(\text{term II}/\text{term I}) \approx 3.36 \times 10^{-5} \text{ m}^{-1}$  and  $L = 2\pi/K_l = 187$  km, which satisfied the short-wavelength assumption. Additional observations are required for detailed research on 10–20-day meridional oscillations in subthermocline and the vertical trapping scale of bottom TRWs in the future.

### 5. Summary

Based on the over 3 years of velocity records, we observed deep current variability with a typical period of 10–20 days in the eastern off-equatorial Indian Ocean, accounting for over

50% of the total bottom subtidal velocity variability. These deep oscillations are more energetic in the cross-isobathic direction ( $\text{STD} = 3.02 \text{ cm s}^{-1}$ ) than in the along-isobathic direction ( $\text{STD} = 1.50 \text{ cm s}^{-1}$ ), with maximum amplitude of  $10.71 \text{ cm s}^{-1}$  ( $5.63 \text{ cm s}^{-1}$ ) in the cross-slope (along-slope) direction. Considering the smaller value of the Coriolis parameter and the stronger  $\beta$  effect at low latitude, we obtain the TRW dispersion relation (i.e.,  $\omega = [N|\nabla h| \sin\theta/\tanh(\lambda h)]\{\sqrt{1 - (\omega^2/f_0^2)}\sqrt{1 + [\beta k/(\omega K^2)]}\}$ ) in the subtropical region, which is applicable in the situation that the motions are high frequency and planetary  $\beta$  is comparable to the topographic  $\beta$  (i.e.,  $\beta_{\text{Topo}}$ ). The 10–20-day deep oscillations are interpreted as TRWs because they satisfy the dispersion relation. Our correlation analysis suggested that these deep oscillations were closely linked to the upper-layer 10–20-day perturbations in the cross-isobathic direction, which were energetic in the subthermocline at the depths of 300–950 m but weak near the surface. Further EOF decomposition and time-lag correlation analysis proved that the observed subthermocline cross-isobathic oscillations acted as the energy source of TRW variability, adjusting deep cross-isobathic currents through the barotropic mode (i.e., the first EOF). Therefore, the observed  $\sim 11$ -day TRWs were generated by cross-isobathic motions under PV conservation adjustment.

The MO model output could reproduce the observed 10–20-day bottom current variability, and were therefore used to discuss deep-sea energetics. Applying MS-EVA to the MO output from 2014 to 2019, the vertical and horizontal pressure work were identified as the dominant source and sink of energy of the deep-ocean variability, respectively. In the entire off-equatorial seamount region ( $2^\circ\text{--}10^\circ\text{N}$ ,  $89^\circ\text{--}92^\circ\text{E}$ ), the primary source of energy for deep-current variability was the vertical pressure work, which transported energy downward and accounted for approximately 94% of the total  $K^1$  sources. The deep-layer  $K^1$  was redistributed by the horizontal pressure work process, which contributed approximately 98% of the total  $K^1$  sinks.

*Acknowledgments.* This work was supported by the National Natural Science Foundation of China (42076019, 42206033, 42176021), the Open Project Program of State Key Laboratory of Tropical Oceanography (Project LTOZZ2001), Basic Frontiers and Innovative Development 2023 “Integration” Project of South China Sea Institute of Oceanology (SCSIO2023QY02).

*Data availability statement.* The AVISO data are available at <https://www.aviso.altimetry.fr>. The bathymetry and WOA18 data can be obtained at <http://apdrc.soest.hawaii.edu/> and <https://www.nodc.noaa.gov/OC5/woa18>, respectively. Mercator Ocean reanalysis output can be obtained at [https://resources.marine.copernicus.eu/product-detail/GLOBAL\\_MULTIYEAR\\_PHY\\_001\\_030](https://resources.marine.copernicus.eu/product-detail/GLOBAL_MULTIYEAR_PHY_001_030).

## REFERENCES

- Amante, C., and B. W. Eakins, 2009: ETOPO1 global relief model converted to PanMap layer format. PANGAEA, accessed 1 May 2022, <https://doi.org/10.1594/PANGAEA.769615>.
- Arzeno, I. B., S. N. Giddings, G. Pawlak, and R. Pinkel, 2020: Generation of quasi-biweekly Yanai waves in the equatorial Indian Ocean. *Geophys. Res. Lett.*, **47**, e2020GL088915, <https://doi.org/10.1029/2020GL088915>.
- Chatterjee, A., D. Shankar, J. P. McCreary Jr., and P. N. Vinayachandran, 2013: Yanai waves in the western equatorial Indian Ocean. *J. Geophys. Res. Oceans*, **118**, 1556–1570, <https://doi.org/10.1002/jgrc.20121>.
- Chen, G., W. Han, Y. Li, M. J. McPhaden, J. Chen, W. Wang, and D. Wang, 2017: Strong intraseasonal variability of meridional currents near  $5^\circ\text{N}$  in the eastern Indian Ocean: Characteristics and causes. *J. Phys. Oceanogr.*, **47**, 979–998, <https://doi.org/10.1175/JPO-D-16-0250.1>.
- Chen, J., X.-H. Zhu, H. Zheng, H. Nakamura, R. Zhao, M. Wang, J.-H. Park, and A. Nishina, 2022: Observation of topographic Rossby waves triggered by Kuroshio path meander in the East China Sea. *J. Geophys. Res. Oceans*, **127**, e2022JC018667, <https://doi.org/10.1029/2022JC018667>.
- Cheng, X., S.-P. Xie, J. P. McCreary, Y. Qi, and Y. Du, 2013: Intraseasonal variability of sea surface height in the Bay of Bengal. *J. Geophys. Res. Oceans*, **118**, 816–830, <https://doi.org/10.1002/jgrc.20075>.
- Ducet, N., P. Y. Le Traon, and G. Reverdin, 2000: Global high-resolution mapping of ocean circulation from TOPEX/Poseidon and ERS-1 and -2. *J. Geophys. Res.*, **105**, 19477–19498, <https://doi.org/10.1029/2000JC900063>.
- Girishkumar, M. S., M. Ravichandran, and M. J. McPhaden, 2013: Temperature inversions and their influence on the mixed layer heat budget during the winters of 2006–2007 and 2007–2008 in the Bay of Bengal. *J. Geophys. Res. Oceans*, **118**, 2426–2437, <https://doi.org/10.1002/jgrc.20192>.
- Hamilton, P., 1990: Deep currents in the Gulf of Mexico. *J. Phys. Oceanogr.*, **20**, 1087–1104, [https://doi.org/10.1175/1520-0485\(1990\)020<1087:DCITGO>2.0.CO;2](https://doi.org/10.1175/1520-0485(1990)020<1087:DCITGO>2.0.CO;2).
- , 2007: Deep-current variability near the Sigsbee Escarpment in the Gulf of Mexico. *J. Phys. Oceanogr.*, **37**, 708–726, <https://doi.org/10.1175/JPO2998.1>.
- , 2009: Topographic Rossby waves in the Gulf of Mexico. *Prog. Oceanogr.*, **82**, 1–31, <https://doi.org/10.1016/j.pocean.2009.04.019>.
- Hendon, H. H., and J. Glick, 1997: Intraseasonal air–sea interaction in the tropical Indian and Pacific Oceans. *J. Climate*, **10**, 647–661, [https://doi.org/10.1175/1520-0442\(1997\)010<0647:IASIIT>2.0.CO;2](https://doi.org/10.1175/1520-0442(1997)010<0647:IASIIT>2.0.CO;2).
- Hogg, N. G., 2000: Low-frequency variability on the western flanks of the Grand Banks. *J. Mar. Res.*, **58**, 523–545, <https://doi.org/10.1357/002224000321511007>.
- Huang, K., and Coauthors, 2018: Vertical propagation of mid-depth zonal currents associated with surface wind forcing in the equatorial Indian Ocean. *J. Geophys. Res. Oceans*, **123**, 7290–7307, <https://doi.org/10.1029/2018JC013977>.
- , D. Wang, W. Han, M. Feng, G. Chen, W. Wang, J. Chen, and J. Li, 2019: Semiannual variability of middepth zonal currents along  $5^\circ\text{N}$  in the eastern Indian Ocean: Characteristics and causes. *J. Phys. Oceanogr.*, **49**, 2715–2729, <https://doi.org/10.1175/JPO-D-19-0089.1>.
- , and Coauthors, 2020: Baroclinic characteristics and energetics of annual Rossby waves in the southern tropical Indian Ocean. *J. Phys. Oceanogr.*, **50**, 2591–2607, <https://doi.org/10.1175/JPO-D-19-0294.1>.
- Johns, W. E., and D. R. Watts, 1986: Time scales and structure of topographic Rossby waves and meanders in the deep Gulf

- Stream. *J. Mar. Res.*, **44**, 267–290, <https://doi.org/10.1357/002224086788405356>.
- Lellouche, J.-M., and Coauthors, 2018: Recent updates to the Copernicus Marine Service global ocean monitoring and forecasting real-time 1/12° high-resolution system. *Ocean Sci.*, **14**, 1093–1126, <https://doi.org/10.5194/os-14-1093-2018>.
- Liang, X. S., 2016: Canonical transfer and multiscale energetics for primitive and quasigeostrophic atmospheres. *J. Atmos. Sci.*, **73**, 4439–4468, <https://doi.org/10.1175/JAS-D-16-0131.1>.
- , and A. R. Robinson, 2005: Localized multiscale energy and vorticity analysis: I. Fundamentals. *Dyn. Atmos. Oceans*, **38**, 195–230, <https://doi.org/10.1016/j.dynatmoce.2004.12.004>.
- , and D. G. M. Anderson, 2007: Multiscale window transform. *Multiscale Model. Simul.*, **6**, 437–467, <https://doi.org/10.1137/06066895X>.
- , and A. R. Robinson, 2007: Localized multi-scale energy and vorticity analysis: II. Finite-amplitude instability theory and validation. *Dyn. Atmos. Oceans*, **44**, 51–76, <https://doi.org/10.1016/j.dynatmoce.2007.04.001>.
- , and —, 2009: Multiscale processes and nonlinear dynamics of the circulation and upwelling events off Monterey Bay. *J. Phys. Oceanogr.*, **39**, 290–313, <https://doi.org/10.1175/2008JPO3950.1>.
- Ma, J., and X. S. Liang, 2017: Multiscale dynamical processes underlying the wintertime Atlantic blockings. *J. Atmos. Sci.*, **74**, 3815–3831, <https://doi.org/10.1175/JAS-D-16-0295.1>.
- Ma, Q., F. Wang, J. Wang, and Y. Lyu, 2019: Intensified deep ocean variability induced by topographic Rossby waves at the Pacific Yap-Mariana junction. *J. Geophys. Res. Oceans*, **124**, 8360–8374, <https://doi.org/10.1029/2019JC015490>.
- Ma, Y., D. Wang, Y. Shu, J. Chen, Y. He, and Q. Xie, 2022: Bottom-reached near-inertial waves induced by the tropical cyclones, Conson and Mindulle, in the South China Sea. *J. Geophys. Res. Oceans*, **127**, e2021JC018162, <https://doi.org/10.1029/2021JC018162>.
- Madden, R. A., and P. R. Julian, 1971: Detection of a 40–50 day oscillation in the zonal wind in the tropical Pacific. *J. Atmos. Sci.*, **28**, 702–708, [https://doi.org/10.1175/1520-0469\(1971\)028<0702:DOADOI>2.0.CO;2](https://doi.org/10.1175/1520-0469(1971)028<0702:DOADOI>2.0.CO;2).
- Maslo, A., J. M. A. C. de Souza, and J. S. Pardo, 2020: Energetics of the deep Gulf of Mexico. *J. Phys. Oceanogr.*, **50**, 1655–1675, <https://doi.org/10.1175/JPO-D-19-0308.1>.
- Masumoto, Y., H. Hase, Y. Kuroda, H. Matsuura, and K. Takeuchi, 2005: Intraseasonal variability in the upper layer currents observed in the eastern equatorial Indian Ocean. *Geophys. Res. Lett.*, **32**, L02607, <https://doi.org/10.1029/2004GL021896>.
- Miyamoto, M., and Coauthors, 2020: Topographic Rossby waves at two different periods in the northwest Pacific basin. *J. Phys. Oceanogr.*, **50**, 3123–3139, <https://doi.org/10.1175/JPO-D-19-0314.1>.
- Oey, L.-Y., and H.-C. Lee, 2002: Deep eddy energy and topographic Rossby waves in the Gulf of Mexico. *J. Phys. Oceanogr.*, **32**, 3499–3527, [https://doi.org/10.1175/1520-0485\(2002\)032<3499:DEEATR>2.0.CO;2](https://doi.org/10.1175/1520-0485(2002)032<3499:DEEATR>2.0.CO;2).
- Quan, Q., Z. Cai, G. Jin, and Z. Liu, 2021a: Topographic Rossby waves in the abyssal South China Sea. *J. Phys. Oceanogr.*, **51**, 1795–1812, <https://doi.org/10.1175/JPO-D-20-0187.1>.
- , Z. Liu, S. Sun, Z. Cai, Y. Yang, G. Jin, Z. Li, and X. S. Liang, 2021b: Influence of the Kuroshio intrusion on deep flow intraseasonal variability in the northern South China Sea. *J. Geophys. Res. Oceans*, **126**, e2021JC017429, <https://doi.org/10.1029/2021JC017429>.
- , —, Y. Yang, Z. Cai, H. Zhang, and X. Liu, 2022: Characterization of intraseasonal fluctuations in the abyssal South China Sea: An insight into the energy pathway. *Prog. Oceanogr.*, **206**, 102829, <https://doi.org/10.1016/j.pcean.2022.102829>.
- Rhines, P., 1970: Edge-, bottom-, and Rossby waves in a rotating stratified fluid. *Geophys. Fluid Dyn.*, **1**, 273–302, <https://doi.org/10.1080/03091927009365776>.
- Schott, F., J. Reppin, J. Fischer, and D. Quadfasel, 1994: Currents and transports of the monsoon current south of Sri Lanka. *J. Geophys. Res.*, **99**, 25 127–25 141, <https://doi.org/10.1029/94JC02216>.
- Sengupta, D., R. Senan, V. S. N. Murty, and V. Fernando, 2004: A biweekly mode in the equatorial Indian Ocean. *J. Geophys. Res.*, **109**, C10003, <https://doi.org/10.1029/2004JC002329>.
- Shin, J., S. Noh, and S. Nam, 2020: Intraseasonal abyssal current variability of bottom-trapped topographic Rossby waves in the southwestern East Sea (Japan Sea). *Front. Mar. Sci.*, **7**, 579680, <https://doi.org/10.3389/fmars.2020.579680>.
- Shinoda, T., T. G. Jensen, M. Flatau, and S. Chen, 2013: Surface wind and upper-ocean variability associated with the Madden-Julian oscillation simulated by the Coupled Ocean–Atmosphere Mesoscale Prediction System (COAMPS). *Mon. Wea. Rev.*, **141**, 2290–2307, <https://doi.org/10.1175/MWR-D-12-00273.1>.
- Shu, Y., and Coauthors, 2016: Persistent and energetic bottom-trapped topographic Rossby waves observed in the southern South China Sea. *Sci. Rep.*, **6**, 24338, <https://doi.org/10.1038/srep24338>.
- , and Coauthors, 2022: Deep-current intraseasonal variability interpreted as topographic Rossby waves and deep eddies in the Xisha Islands of the South China Sea. *J. Phys. Oceanogr.*, **52**, 1415–1430, <https://doi.org/10.1175/JPO-D-21-0147.1>.
- Thompson, R., 1971: Topographic Rossby waves at a site north of the Gulf Stream. *Deep-Sea Res. Oceanogr. Abstr.*, **18**, 1–19, [https://doi.org/10.1016/0011-7471\(71\)90011-8](https://doi.org/10.1016/0011-7471(71)90011-8).
- , and J. R. Luyten, 1976: Evidence for bottom-trapped topographic Rossby waves from single moorings. *Deep-Sea Res. Oceanogr. Abstr.*, **23**, 629–635, [https://doi.org/10.1016/0011-7471\(76\)90005-X](https://doi.org/10.1016/0011-7471(76)90005-X).
- Wang, D., and Coauthors, 2019: Advances in research of the mid-deep South China Sea circulation. *Sci. China Earth Sci.*, **62**, 1992–2004, <https://doi.org/10.1007/s11430-019-9546-3>.
- Wang, J., and Coauthors, 2021: Observed variability of bottom-trapped topographic Rossby waves along the slope of the northern South China Sea. *J. Geophys. Res. Oceans*, **126**, e2021JC017746, <https://doi.org/10.1029/2021JC017746>.
- Wang, Q., and Coauthors, 2019: Energetic topographic Rossby waves in the northern South China Sea. *J. Phys. Oceanogr.*, **49**, 2697–2714, <https://doi.org/10.1175/JPO-D-18-0247.1>.
- Webster, P. J., and Coauthors, 2002: The JASMINE pilot study. *Bull. Amer. Meteor. Soc.*, **83**, 1603–1630, <https://doi.org/10.1175/BAMS-83-11-1603>.
- Yang, Y., and X. S. Liang, 2019: New perspectives on the generation and maintenance of the Kuroshio large meander. *J. Phys. Oceanogr.*, **49**, 2095–2113, <https://doi.org/10.1175/JPO-D-18-0276.1>.
- , R. H. Weisberg, Y. Liu, and X. S. Liang, 2020: Instabilities and multiscale interactions underlying the loop current eddy shedding in the Gulf of Mexico. *J. Phys. Oceanogr.*, **50**, 1289–1317, <https://doi.org/10.1175/JPO-D-19-0202.1>.
- , X. S. Liang, and H. Sasaki, 2021: Vertical coupling and dynamical source for the intraseasonal variability in the deep Kuroshio Extension. *Ocean Dyn.*, **71**, 1069–1086, <https://doi.org/10.1007/s10236-021-01482-9>.

- Zhao, B., and M.-L. Timmermans, 2018: Topographic Rossby waves in the Arctic Ocean's Beaufort Gyre. *J. Geophys. Res. Oceans*, **123**, 6521–6530, <https://doi.org/10.1029/2018JC014233>.
- Zheng, H., C. Zhang, R. Zhao, X.-H. Zhu, Z.-N. Zhu, Z.-J. Liu, and M. Wang, 2021a: Structure and variability of abyssal current in northern South China Sea based on CPIES observations. *J. Geophys. Res. Oceans*, **126**, e2020JC016780, <https://doi.org/10.1029/2020JC016780>.
- , X.-H. Zhu, C. Zhang, R. Zhao, Z.-N. Zhu, and Z.-J. Liu, 2021b: Propagation of topographic Rossby waves in the deep basin of the South China Sea based on abyssal current observations. *J. Phys. Oceanogr.*, **51**, 2783–2791, <https://doi.org/10.1175/JPO-D-21-0051.1>.
- Zhu, Y., and X. Liang, 2020: Coupling of the surface and near-bottom currents in the Gulf of Mexico. *J. Geophys. Res. Oceans*, **125**, e2020JC016488, <https://doi.org/10.1029/2020JC016488>.